HHS Public Access

Author manuscript

*J Control Release*. Author manuscript; available in PMC 2019 August 10.

Published in final edited form as:

*J Control Release*. 2018 August 10; 283: 143–150. doi:10.1016/j.jconrel.2018.05.039.

# Focused ultrasound-enabled delivery of radiolabeled nanoclusters to the pons

**Dezhuang Ye**[a,#], **Deborah Sultan**[b,#], **Xiaohui Zhang**[b], **Yimei Yue**[c], **Gyu Seong Heo**[b], **Satya V.V.N. Kothapalli**[c], **Hannah Luehmann**[b], **Yuan-chuan Tai**[b], **Joshua B. Rubin**[d], **Yongjian Liu**[b,*], and **Hong Chen**[c,*]

[a]Department of Mechanical Engineering and Material Science, Washington University in St. Louis, Saint Louis, Missouri, 63130, USA

[b]Mallinckrodt Institute of Radiology, Washington University School of Medicine, St. Louis, Missouri 63110, USA

[c]Department of Biomedical Engineering, Washington University in St. Louis, Saint Louis, Missouri, 63130, USA

[d]Department of Pediatrics, Department of Neuroscience, Washington University School of Medicine, St. Louis, Missouri 63110, USA

## Abstract

The goal of this study was to establish the feasibility of integrating focused ultrasound (FUS)-mediated delivery of $^{64}$Cu-integrated gold nanoclusters ($^{64}$Cu-AuNCs) to the pons for *in vivo* quantification of the nanocluster brain uptake using positron emission tomography (PET) imaging. FUS was targeted at the pons for the blood-brain barrier (BBB) disruption in the presence of systemically injected microbubbles, followed by the intravenous injection of $^{64}$Cu-AuNCs. The spatiotemporal distribution of the $^{64}$Cu-AuNCs in the brain was quantified using *in vivo* microPET/CT imaging at different time points post injection. Following PET imaging, the accumulation of radioactivity in the pons was further confirmed using autoradiography and gamma counting, and the gold concentration was quantified using inductively coupled plasma-mass spectrometry (ICP-MS). We found that the noninvasive and localized BBB opening by the FUS can successfully deliver the $^{64}$Cu-AuNCs to the pons. We also demonstrated that *in vivo* real-time microPET/CT imaging was a reliable method for monitoring and quantifying the brain uptake of $^{64}$Cu-AuNCs delivered by the FUS. This drug delivery platform that integrates FUS, radiolabeled nanoclusters, and PET imaging provides a new strategy for noninvasive and localized nanoparticle delivery to the pons with concurrent *in vivo* quantitative imaging to evaluate delivery efficiency. The long-term goal is to apply this drug delivery platform to the treatment of pontine gliomas.

[*]Address correspondence to: Yongjian Liu, Mallinckrodt Institute of Radiology, Washington University School of Medicine, St. Louis, Missouri 63110, USA. yongjianliu@wustl.edu. Hong Chen, Ph.D., Department of Biomedical Engineering and Radiation Oncology, Washington University in St. Louis. 4511 Forest Park Ave. St. Louis, MO, 63108, USA. hongchen@wustl.edu.
[#]Dezhuang Ye and Deborah Sultan contributed equally to this work.

**Keywords**

Focused ultrasound; Nanoclusters; Brain; Pons; Blood-brain barrier; Positron emission tomography; Drug delivery; Image-guided drug delivery

## I. Introduction

Pediatric brain tumors kill more children than any other cancers, including leukemia. Among all pediatric brain tumors, diffuse intrinsic pontine glioma (DIPG) is the most common brainstem tumor of childhood and the single greatest cause of brain tumor-related death in children [1,2]. The treatment outcomes of DIPG have not been improved for decades, which is associated with two unique characteristics of DIPG. First, the pons is one of the major structures in the brainstem that controls basic vital life functions, such as breathing, hearing, taste, balance, and communication between different parts of the brain. The critical anatomic location of the pons precludes surgical intervention and limits the use of other invasive therapeutic techniques. Second, in contrast to gliomas elsewhere in the brain, which often have compromised blood-brain barrier/blood-tumor barrier (BBB/BTB), the BBB/BTB in DIPG is frequently intact as suggested by the lack of contrast enhancement after magnetic resonance imaging (MRI) contrast agent administration [3]. Currently, ongoing phase I/II clinical trials seek to circumvent BBB/BTB function in DIPG using convection-enhanced drug delivery [4]. However, the invasive implantation of catheters for convection-enhanced drug delivery raises significant safety concerns. Thus, there is a pressing need for the development of alternative, noninvasive techniques for BBB/BTB disruption for efficient delivery of chemotherapy to the pons for the treatment of DIPG.

Transcranial focused ultrasound (FUS) in combination with microbubbles has been established as a promising technique for noninvasive and localized BBB opening. FUS concentrates externally generated ultrasound waves through the intact scalp and skull onto cubic millimeter-sized regions up to ~10 cm deep into the brain, allowing highly precise and noninvasive targeting of focal brain locations. Microbubbles, gas-filled micron-sized bubbles coated by shells, are constrained in the vasculature after intravenous administration, as their sizes are comparable to red blood cells. When the microbubbles are exposed to the FUS, they undergo volumetric oscillation, which generates mechanical forces on the endothelium and results in a transient increase in the BBB permeability. The strategy of combining FUS with microbubbles for drug delivery across the BBB was first reported more than a decade ago [5]. Subsequent studies in rodent and non-human primates have confirmed that FUS can induce temporary BBB opening without observable tissue damage or functional deficits even after repeated administration [6–8]. Increased therapeutic efficacy of various agents delivered by the FUS technique has also been demonstrated [9–11]. Despite the great advancement of the FUS technique, its application has been focused on the treatment of diseases located within the cerebrum (*e.g.*, glioblastoma and Alzheimer's disease). However, pediatric brain tumors are commonly located in the cerebellum and brain stem, which are rare sites for adult brain tumors. The application of FUS-enhanced drug delivery to these brain locations has not been studied [12].

Recently, there has been a growing interest in using FUS for the trans-BBB delivery of nanoparticles, which takes advantage of the noninvasive and localized BBB disruption capability of FUS and the unique characteristics of nanoparticles as multicomponent constructs containing imaging, targeting, and therapeutic entities. For example, it was demonstrated that FUS sonication enhanced the delivery of chemotherapeutic drug-loaded liposomes and significantly hindered the brain tumor growth in a mouse model [13]. One study showed the successful trans-BBB delivery of a biodegradable polymeric nanoparticle that is capable of penetrating within the brain microenvironment [14]. Magnetic nanoparticles were also delivered by FUS-induced BBB opening, and the deposition of the magnetic nanoparticles at the targeted brain site was enhanced by magnetic targeting with concurrent MRI monitoring [10]. In another study, gold nanoparticles were safely delivered to the tumor margins in a mouse brain tumor model [15]. Recently, low-density lipoprotein nanoparticles reconstituted with docosahexaenoic acid (DHA) were delivered to the brain by the FUS-induced BBB opening technique and led to the enhanced delivery of DHA in the exposure region of the brain [11]. Among all the previously reported studies, only one study delivered radiolabeled-nanoparticles [16]. In that study, $^{111}$In-labeled liposomes, which were conjugated with human atherosclerotic plaque-specific peptide-1 (AP-1) and loaded with doxorubicin, were imaged using single-photon emission computed tomography (SPECT), from which the tumor-to-normal brain ratio of the liposome concentration was calculated. Recently, ultrasmall nanoclusters have drawn significant attention for biomedical applications due to their size-promoted clearance after systematic injection [17–21], and accurate tumor targeting as we demonstrated in previous research [22]. Through direct $^{64}$Cu incorporation into the structure of gold nanocluster ($^{64}$Cu-AuNCs), quantitative pharmacokinetic analysis by PET imaging can be performed to determine the penetration and retention of $^{64}$Cu-AuNCs in tissue.

The goal of this study was to demonstrate successful delivery of ultrasmall $^{64}$Cu-AuNCs in the pons by FUS-mediated BBB opening and to quantify the *in vivo* spatiotemporal distribution of $^{64}$Cu-AuNCs using PET imaging. We first investigated the feasibility of FUS-mediated delivery of a model drug to the pons by disrupting the BBB. We then investigated the FUS-mediated delivery of $^{64}$Cu-AuNCs to the pons and monitored the spatiotemporal distribution of $^{64}$Cu-AuNCs with PET imaging. The successful delivery of $^{64}$Cu-AuNCs into the pons was verified by autoradiography and gamma counting of *ex vivo* brain slices and ICP-MS measurement of gold concentration in the pons. The data presented here demonstrate the feasibility of this combined approach for effective and quantitative delivery of $^{64}$Cu-AuNCs into pons.

## 2. Materials and methods

### 2.1. Animals

All animal procedures for these experiments were reviewed and approved by the Institutional Animal Care and Use Committee of Washington University in St. Louis in accordance with the National Institutes of Health Guidelines for animal research. Adult male mice (C57BL/6, age 6 to 8 weeks, Charles River Laboratory, Wilmington, MA, USA) were divided into four groups: Group 1 (n=3) evaluated the delivery of a model drug across the

BBB into the pons after FUS treatment; Group 2 (n=3) evaluated the safety of the FUS treatment; Group 3 (n=8) assessed FUS-enabled delivery of $^{64}$Cu-AuNCs to the pons using *in vivo* microPET/CT imaging; Group 4 (n=12) verified *in vivo* imaging results with *ex vivo* autoradiography, gamma counting, and inductively coupled plasma mass spectrometry (ICP-MS).

### 2.2. FUS sonication

An ultrasound image-guided FUS system (VIFU 2000, Alpinion US Inc., Bothell, WA, USA) was used for the sonication (Fig. 1A). The FUS transducer had a center frequency of 1.5 MHz, a focal depth of 60 mm, an aperture of 60 mm, a circular central opening of 38 mm, and was driven by a built-in signal generator. The transducer was connected to a 3D stage for positioning (Velmex, Lachine, QC, Canada). The transducer was also attached to a water balloon filled with degassed water to provide acoustic coupling. The water balloon was immersed in a degassed water container, the bottom of which featured a window sealed with an acoustically and optically transparent membrane (Tegaderm, 3M, St. Paul, MN, USA). A B-mode imaging probe (L8–14, working frequency 8–14 MHz, center frequency 12 MHz, Alpinion, Seoul, Korea) was inserted into the FUS transducer opening and aligned with the focal plane. Mice were placed prone on a heating pad with their heads immobilized by a stereotaxic frame (David Kopf Instruments, Tujunga, CA, USA). The fur on the head was removed while the skull and the scalp remained intact. The water container was placed on the mouse head and coupled with degassed ultrasound gel.

The pressure amplitudes and beam dimensions of the FUS transducer were calibrated using a needle hydrophone (Onda, CA, USA) in a degassed water tank before the experiment. The pressures reported here were the measured hydrophone peak negative pressures with corrections for mouse skull attenuation [23]. The pressure field measured in the axial plane is shown in Figure 1B. The full width at half maximum (FWHM) of the axial beam (Figure 1C) and lateral beam (Figure 1D) were 6.04 mm and 0.62 mm, respectively.

Targeting the FUS focus at the pons was performed with the assistance of a grid. The grid was positioned in the water container on top of the mouse head with the crossing point in alignment with the lambda, an anatomic landmark on the skull and visible through the mouse skin on the head. The B-mode imaging probe was used to scan through the grid and form a 3D image of the grid using a customized Matlab (Mathworks inc., Natick, MA, USA) program. The crossing point of the grid was then identified and used as the reference point for targeting the FUS to the pons on the left side of the mouse brain based on the pons' stereotactic location relative to the lambda (0 mm frontal and 1.50 mm to the left). The depth of FUS focus was adjusted to be 4.00 mm from the skull by measuring the distance from the skull on the B-mode images.

Size-selected microbubbles with a median diameter of 4–5 μm were prepared in-house according to a previously described protocol [24] and diluted using sterile saline to a final concentration of approximately $8\times10^8$ number of microbubbles per mL. The diluted microbubbles (volume = 25 μL) were administered through a bolus injection *via* the tail vein. Immediately after injection (~9 s), pulsed FUS (center frequency 1.5 MHz; pressure 0.52 MPa; pulse length 0.67 ms; pulse repetition frequency 5 Hz; duration 1 min) was

applied to the left side of the pons. The pressure reported here was the peak negative pressure measured in water with correction for mouse skull attenuation (18%) [27].

A Texas red-tagged dextran (amount 2 mg, molecular weight 40 kDa, Invitrogen, Carlsbad, CA, USA) was dissolved in 100 μL saline and co-injected with the microbubbles to mice in group 1. The mean hydrodynamic diameter ($D_H$) of the dextran as measured using dynamic light scattering (NanoZS, Malvern, Worcestershire, UK) was 4.10 nm. Microbubbles mixed with 100 μL saline were injected to the mice in group 2. The mice in the treatment subgroup of group 3 were injected with $^{64}$Cu-AuNCs mixed with 60 μL Evans blue at 1 h post FUS sonication. Evans blue was used to provide a visual indication of the BBB opening location.

### 2.3. Fluorescence imaging and quantification

Mice in group 1 were transcardially perfused at 4 h post-FUS sonication, and their brains were harvested. After overnight fixation in paraformaldehyde followed by cryoprotection with sucrose, the brains were cut into transverse sections and imaged using a fluorescence microscope (Axi-overt S100; Zeiss, Oberkochen, Germany). For each mouse, a customized Matlab program was used to quantify the fluorescent signal in 15 sequential brain slices. Circles with a 2-mm diameter were selected by the Matlab program on the left and right sides of the pons as the regions of interests (ROIs). The background autofluorescence intensity was calculated by the mean + 3× standard deviation of the pixel intensity within the non-treated right-side ROI. Pixels with intensities above the background autofluorescence intensity were identified within both the left- and right-side ROIs. The mean fluorescence intensities of those identified pixels within the left- and right-side ROIs were calculated to represent the relative amount of dextran delivered to the FUS-treated and non-treated pons, respectively.

### 2.4. Histological analysis

For mice in group 2, whole brain histologic examinations were performed using hematoxylin and eosin (H&E) staining. The harvested animal brains were fixed in 4% paraformaldehyde, embedded in paraffin, and sectioned horizontally at 6 μm thickness in 10 separate levels with 180 μm intervals between two adjacent levels. At each level, four sections were acquired and stained with H&E. Histological evaluation was performed single blinded, by a trained observer without knowledge of the location and parameters of sonication.

### 2.5. Synthesis and characterization of $^{64}$Cu-AuNCs

$^{64}$Cu-AuNCs were synthesized as described previously [21]. In a typical reaction, water (2.0 mL), $HAuCl_4$ (10 mM, 376 μL), and $^{64}CuCl_2$ (74 MBq) were mixed in a glass vial, followed by the dropwise addition of m-dPEG®12-Lipoamide (MW = 750 Da, 10 mM, 400 μL). Sodium borohydride (40 mM, 400 μL) was added to this mixture and stirred rapidly for 2 hours. The $^{64}$Cu-AuNCs were purified using a centrifuge filter (Amicon, 10K). Radiochemical purity was determined using silica impregnated iTLC paper with a mobile phase of 1:1 methanol: 10% ammonium acetate. Transmission electron microscopy (TEM) of decayed nanoclusters utilized a Tecnai G2 Spirit Transmission Electron Microscope operated at 120 kV (FEI, Hillsboro, OR). Additionally, dynamic light scattering (DLS) and

zeta potential measurements were measured using Zetasizer Nano ZS from Malvern Instruments.

### 2.6. In vivo microPET/CT imaging of $^{64}$Cu-AuNCs kinetics in the brain

Four mice in group 3 were treated with FUS followed by intravenous injection of $^{64}$Cu-AuNCs [3.7 MBq (100 μci) in 100 μL of saline/mouse], while the other four mice in group 3 were injected with the same amount of $^{64}$Cu-AuNCs without FUS treatment. MicroPET/CT scans were performed on all mice using the Inveon PET/CT system (Siemens, Malvern, PA) at 1 h, 4 h, and 24 h post injection. The PET images were corrected for attenuation, scatter, normalization, and camera dead time and co-registered with CT images. The amount of activity recorded at the time of imaging was decay corrected for the time between $^{64}$Cu-AuNCs injection and imaging. The PET images were reconstructed with the maximum a posteriori (MAP) algorithm and analyzed using Inveon Research Workplace. The uptake of $^{64}$Cu-AuNCs in the brain was calculated in terms of the percent injected dose per gram (%ID/g) of tissue in three-dimensional regions of interest (ROIs) without the correction for partial volume effect.

### 2.7. $^{64}$Cu-AuNCs biodistribution

Following the 24 h PET scans, animals were sacrificed, and all organs of interest were collected, weighed, and counted in a Beckman 8000 gamma counter (Beckman, Fullerton, CA). The count rate (counts per minute, CPM) from each sample of tissue was corrected by automatic background subtraction and decay corrected (compensated for the decay of $^{64}$Cu radioactivity over time). The corrected CPM from each tissue sample was normalized both to the mass of the tissue sample (in grams, g) and to the injected dose (ID). Thus, the relative concentration of $^{64}$Cu-AuNCs in each tissue sample was calculated as %ID/g.

### 2.8. Ex vivo evaluation of FUS delivery of $^{64}$Cu-AuNCs

Of the 12 mice in group 4, nine were treated by FUS followed by intravenous injection of one of three $^{64}$Cu-AuNCs concentrations: 3.7 MBq, 9.3 MBq, or 18.5 MBq. The FUS treatment protocol was the same as that described in section 2.2. The other four mice in group 4 were intravenously injected with 3.7 MBq of $^{64}$Cu-AuNCs without FUS treatment.

All of the mice in group 4 were sacrificed at 24 h post injection. The excised brains were sliced coronally into 2-mm sections using a brain matrix (RBM-2000C; ASI Instruments, Inc., MI). The slices were placed on a phosphor-imaging plate for overnight exposure. The radioactivity of the brain slices was detected by autoradiography using a Storm 840 Phosphorimager (GE, Marlborough, MA). Then, slices containing the pons were cut into two halves to separate the FUS-treated and non-treated sides. Gamma counting was performed for each piece of tissue samples to detect the $^{64}$Cu radioactivity These samples were then digested using a high-pressure microwave digestion system (Milestone Inc. Monroe, CT) and gold concentration in the digested brain tissue samples was determined using ICP-MS (Elan DRC-e, PerkinElmer, Germany). Additionally, livers from all mice were harvested and prepared to verify the correlation between the detected $^{64}$Cu radioactivity by gamma counting and the gold concentration quantified by ICP-MS.

### 2.9. Statistical analysis

Statistical analysis was performed using GraphPad Prism (Version 6.04, La Jolla, CA, USA). Group variation was described as mean ± standard deviation. Differences among two groups were determined using the unpaired two-tailed Student's t-test. One-way ANOVA analysis followed by a post-hoc Tukey's test was used to exam differences among three groups. A $P$ value < 0.05 was considered to represent a significant difference. Linear curve fitting between the gamma counting and ICP-MS results was carried out using GraphPad and the goodness of fit, $R^2$, was calculated.

## 3. Results

### 3.1. FUS-mediated delivery of a model drug to the pons is precisely targeted and non-invasive

Figure 2A shows a representative fluorescence image of a horizontal slice of the hindbrain containing the pons obtained from a mouse in Group 1. The fluorescently labeled dextran was mainly accumulated in the FUS-treated region of pons with minimal signal observed in the non-treated region. This enhanced delivery of dextran at the FUS-treated pons was consistently observed within this group of mice. Quantification of the *ex vivo* brain slices found that significantly ($P$ <0.005) higher fluorescence intensity at the FUS-treated site than the contralateral non-treated pons (Fig. 2B). The same brain structure in the contralateral hemisphere was not sonicated and acted as a commonly used internal control for quantifying FUS-induced trans-BBB delivery outcome [9,25,26]. Evaluation of brain slices did not show any tissue damage induced by the FUS treatment at the histological level. Figures 2C and 2D display representative H&E staining of a brain slice. No hemorrhage was observed when comparing the stained slices from FUS-treated region and contralateral non-treated region.

### 3.2. FUS-mediated delivery of $^{64}$Cu-AuNCs into the pons

The representative transmission electron microscopy analysis of decayed $^{64}$Cu-AuNCs showed a homogeneous size distribution, confirmed by DLS analysis ($D_H$ = 5.60±0.50 nm, zeta potential = −0.40±0.11 mV) (Fig. 3).

The PET images obtained from the non-treated mice verified that $^{64}$Cu-AuNCs could not cross the intact BBB (Fig. 4A). While the PET images acquired from the FUS-treated mice demonstrated successful delivery of $^{64}$Cu-AuNCs at the FUS-treated pons (Fig. 4B). Compared with the non-treated mice, FUS enhanced the delivery efficiency of $^{64}$Cu-AuNCs within the targeted pons by 3.37, 3.03 and 4.76 folds at 1 h, 4 h, and 24 h, respectively (Fig. 4C). This observation confirmed that FUS could open the BBB in the FUS-targeted region, allowing the localized delivery of 64Cu-AuNCs into the brain tissue. The radioactivity retained in the FUS-treated pons decreased from 1.85±0.15 %ID/g at 1 h, 1.52±0.09 %ID/g at 4 h, to 1.45±0.16 %ID/g at 24 h (Fig. 4D); while, the volume of brain tissues containing radioactivity increased from 0.06±0.02 $cm^3$ at 1 h, 0.10±0.02 $cm^3$ at 4 h, to 0.14±0.02 $cm^3$ at 24 h (Fig. 4E). Significant differences in concentration and volume were found between 1 h and 4 h (P <0.01) and 1 h and 24 h (P <0.05), while no significant difference was found between 4 h and 24 h (P >0.05).

Autoradiography of *ex vivo* brain slices at 24 h post injection verified localized delivery of $^{64}$Cu-AuNCs to the FUS-targeted pons region (Fig. 5A). A corresponding photograph of the slice is presented in Fig. 5B. Evans blue staining, which indicates the location of the BBB opening, was observed mainly at the left side of the brain slice, which matched the strong radioactive signals observed on the corresponding autoradiography slice. We compared the radioactivity of the FUS-treated side with that of the contralateral non-treated side of the slices, as well as radioactivity of non-treated mice with intravenous injection of the same concentration of $^{64}$Cu-AuNCs (3.7 MBq). It was found that the radioactivity of the FUS-treated side was 2.02±0.26 fold higher than that of the non-treated side of the same brain and 3.03±0.63 fold higher than that of the non-treated mice (Fig. 5C). A significant difference was observed between the contralateral non-treated side and non-treated mice, suggesting that at 24 h post injection the $^{64}$Cu-AuNCs diffused from the FUS-treated side to the contralateral non-treated side due to the small volume of the mouse brain.

Figure 6 summarized the post-PET biodistribution profile of $^{64}$Cu-AuNCs, which was performed at 24 h post injection of the $^{64}$Cu-AuNCs. The radioactivity determined in the liver was 6.04±0.72 %ID/g and spleen was 0.78±0.19 %ID/g. We noted that the whole brain uptake of the nanoclusters at the 24 h post injection (0.37±0.10 %ID/g) was less than that quantified based on PET imaging at 24 h post injection (Fig. 4D), because the PET quantification was performed within the FUS targeted region, instead of the whole brain as in the biodistribution analysis.

Previously, we reported the *in vitro* radiolabel stability of $^{64}$Cu integrated gold nanostructures [30]. Herein, we performed ICP-MS measurement of the gold concentration in the same tissue samples after radioactivity decay. As shown in Figure 7, in the representative brain and liver specimens, the gamma counting data (CPM/g) showed good correlation to the gold concentrations (μg/g).

## 4. Discussion

The vital location of the pons and the intact BBB constitute substantial obstacles to the successful treatment of DIPG. Consequently, there is a critical need for noninvasive and localized trans-BBB drug delivery techniques. As a first step toward the long-term goal of developing a drug delivery platform for the treatment of DIPG, we investigated the feasibility of FUS combined with microbubbles for noninvasive and localized delivery of $^{64}$Cu-AuNCs to the pons of mouse brains. We also integrated the FUS delivery with PET imaging for *in vivo* quantitative evaluation of the $^{64}$Cu-AuNCs delivery efficiency and spatiotemporal distribution.

This study is the first to demonstrate successful opening of the BBB in the pons by the FUS technique, enabling trans-BBB delivery of nanoparticles to the pons [28]. To find the precise targeting location for drug delivery to the pons, we started with using a 40 kDa Texas-red labeled dextran as the model drug, which had a comparable mean hydrodynamic size ($D_H$ =4.10 nm) to that of the $^{64}$Cu-AuNCs ($D_H$ =5.60 nm). We showed precise targeting of the left pons (Figs. 2A) without indication of vascular or tissue damage (Figs. 2C and 2D). Since the brainstem controls vital life functions, the parameters of FUS were chosen to avoid

hemorrhage or neuron damage in reference to previous studies [7,29]. Although not the focus of this study, we monitored the behavior of the mice throughout the course of our experiments. All treated mice recovered from anesthesia within 15 min after the FUS treatment was finished. After recovery, no gross changes in drinking, eating, walking, hanging, jumping, or grooming were observed.

The FUS-induced BBB opening technique has been evaluated for the delivery of various nanoparticles with $D_H$ within the range of 10–200 nm, such as liposomes, polymer nanoparticles, magnetic nanoparticles, lipoprotein nanoparticles, and gold nanoparticles. This study involved the unique integration of the FUS technique with radiolabeled nanoclusters for brain drug delivery. $^{64}$Cu-AuNCs are unique in that their size is much smaller than other nanoparticles. In contrast to the organ uptake acquired with 27-nm $^{64}$Cu-AuNPs [30], the 6-nm $^{64}$Cu-AuNCs showed significantly decreased uptake in blood (0.46 ± 0.04%ID/g vs. 5.95 ± 0.45 %ID/g), liver (6.03 ± 0.72%ID/g, 42.9 ± 3.44 %ID/g), and spleen (0.78 ± 0.19%ID/g vs. 203 ± 11.1%ID/g), suggesting the advantages of renal-clearable nanoclusters in reducing any potential toxicity concerns. [21]. Meanwhile, in our previous study, we used fluorescently-labeled dextrans with various hydrodynamic diameters (2.3 nm, 10.2 nm, 30.6 nm, and 54.4 nm) to evaluate the size-dependency of the FUS-mediated delivery of dextrans to the brain. We found that the smaller dextrans could be delivered to the brain with higher efficiency than the larger dextrans. The delivery of dextrans smaller than 30.6 nm was found to be safe without any detectable tissue damage since lower acoustic pressure was needed for the delivery of smaller agents. In addition, we found a direct correlation between particle size and delivery efficiency, with smaller particles more effectively delivered across the BBB [29]. The succesful delivery of large particles requires higher acounstic energy, which was reported to be associated with tissue damages [9,13]. Thus, the small size of $^{64}$Cu-AuNCs makes them particularly well-suited for pons drug delivery considering the specific location and vital function of the pons. Our preliminary safety evaluation using H&E staining showed no histological-level tissue damage associated with the FUS treatment (Figs. 2C and 2D). Future study is needed to fully evaluate the short-term and long-term safety of the FUS treatment in the pons at both histological and molecular levels [31].

The unique advantage of nanomedicine enables the integration of therapy with imaging. PET imaging of radiolabeled nanoclusters provides a noninvasive, highly sensitive, and quantitative method for assessing the efficiency of nanoparticle delivery and their spatial distribution. Thus, we used PET imaging for the *in vivo* real-time quantification of nanoclusters delivery kinetics. Compared with the non-treated mice, FUS significantly enhanced the delivery efficiency of $^{64}$Cu-AuNCs within the targeted pons (Figs. 4A, 4B, and 4C). The $^{64}$Cu-AuNCs reached the highest concentration in the pons at 1 h post injection and then decreased over time (Fig. 4D), which is consistent with our previous finding that the half-life of the $^{64}$Cu-AuNCs in blood is around 0.87 h [21]. The $^{64}$Cu-AuNCs that were retained in the brain tissue diffused to the surrounding area over time (Fig. 4E). The *ex vivo* autoradiography verified localized delivery of $^{64}$Cu-AuNCs at the FUS-treated region of the pons (Fig. 5A). Gamma counting of *ex vivo* brain slices confirmed the successful delivery of $^{64}$Cu-AuNCs into the pons following FUS treatment and found the ratio between the radioactivity of the treated and non-treated mice were 3.03±0.63 (Fig. 5C). The strong linear

correlation between gamma counting of radioactivity and ICP-MS quantification of Au concentration shown in Fig. 7 confirmed the *in vivo* radiolabel stability of $^{64}$Cu for accurate measurement of $^{64}$Cu-AuNCs organ distribution and uptake.

Although several imaging techniques have been used for *in vivo* imaging of FUS-induced BBB opening, PET has not been used for the *in vivo* quantification of the FUS trans-BBB delivery efficiency of nanoparticles. Our study confirmed that the *in vivo* PET imaging is a reliable imaging method for monitoring and quantifying FUS-enabled delivery of $^{64}$Cu-AuNCs in mice. Several studies have reported *in vivo* PET imaging for the quantification of FUS-enhanced brain delivery of radiolabeled small molecular weight tracers, such as $^{99m}$Tc-diethylenetriaminepentaacetic acid ($^{99m}$Tc-DTPA) [32], integrin α2β1 [33], 2-amino-[3-11C]isobutyric acid ([3-11C]AIB) [34], and $^{18}$F-FDG [35]. Along with these previous studies, the nanoclusters reported here may pave the way for the future development of theranostic PET agent for imaging-guided FUS brain drug delivery.

This study has several limitations. First, only one group of FUS parameters was selected in reference to previous publications and found to be effective and safe for the BBB opening. Future studies will fully optimize the FUS treatment at the pons by exploring different FUS parameters and evaluating the short-term and long-term safety associated with the treatment. Second, $^{64}$Cu-AuNCs were injected 1 h post sonication due to the transportation of mice between facilities. Future study will be performed by injecting $^{64}$Cu-AuNCs and microbubbles simultaneously to improve the delivery efficiency. Third, normal mice were used to demonstrate the feasibility of the proposed technique for the noninvasive and localized drug delivery to the pons. Future studies will evaluate the efficacy of this technique using a mouse model of pontine glioma. Fourth, $^{64}$Cu-AuNCs labeled with molecular targeting ligands can be developed in the future to further improve tumor targeting.

## 5. Conclusion

This study demonstrates that FUS in combination with microbubbles can successfully delivery $^{64}$Cu-AuNCs to the pons. The $^{64}$Cu-AuNCs delivery outcome can be quantified through *in vivo* PET imaging. The successfully delivery was further validated by autoradiography, gamma counting, and ICP-MS. This nanomedicine delivery platform that integrates FUS, PET, and $^{64}$Cu-AuNCs offers a new strategy for noninvasive, localized, and quantitative nanomedicine delivery to the pons.

## Acknowledgments

Funding for this project (MC-II-2017-661) was provided by the Children's Discovery Institute of Washington University and St. Louis Children's Hospital. This work was also partially supported by the Washington University Center for Multiple Myeloma Nanotherapy, under the National Institutes of Health award [U54CA199092], and from the Foundation for Barnes-Jewish Hospital. This work was performed in part at the Nano Research Facility (NRF), a member of the National Nanotechnology Infrastructure Network (NNIN), which is supported by the National Science Foundation [ECS-0335765].

## References


1. Goodwin CR, Xu R, Iyer R, Sankey EW, Liu A, Abu-Bonsrah N, Sarabia-Estrada R, Frazier JL, Sciubba DM, Jallo GI. Local delivery methods of therapeutic agents in the treatment of diffuse intrinsic brainstem gliomas. Clin Neurol Neurosurg. 2016; 142:120–127. [PubMed: 26849840]
2. Jansen MHA, van Vuurden DG, Vandertop WP, Kaspers GJL. Diffuse intrinsic pontine gliomas: A systematic update on clinical trials and biology. Cancer Treat Rev. 2012; 38:27–35. [PubMed: 21764221]
3. Tisnado J, Young R, Peck KK, Haque S. Conventional and advanced imaging of diffuse intrinsic pontine glioma. J Child Neurol. 2016; 31:1386–1393. [PubMed: 27071471]
4. Vanan MI, Eisenstat DD. DIPG in children - what can we learn from the past? Front Oncol. 2015; 5:237. [PubMed: 26557503]
5. Hynynen K, McDannold N, Vykhodtseva N, Jolesz FA. Noninvasive MR imaging-guided focal opening of the blood-brain barrier in rabbits. Radiology. 2001; 220:640–646. [PubMed: 11526261]
6. McDannold N, Arvanitis CD, Vykhodtseva N, Livingstone MS. Temporary disruption of the blood-brain barrier by use of ultrasound and microbubbles: safety and efficacy evaluation in rhesus macaques. Cancer Res. 2012; 72:3652–63. [PubMed: 22552291]
7. Baseri B, Choi JJ, Tung Y-S, Konofagou EE. Multi-modality safety assessment of blood-brain barrier opening using focused ultrasound and definity microbubbles: a short-term study. Ultrasound Med Biol. 2010; 36:1445–59. [PubMed: 20800172]
8. Aryal M, Vykhodtseva N, Zhang Y-Z, McDannold N. Multiple sessions of liposomal doxorubicin delivery via focused ultrasound mediated blood–brain barrier disruption: A safety study. J Control Release. 2015; 204:60–69. [PubMed: 25724272]
9. Etame AB, Diaz RJ, Reilly MAO, Smith CA, Mainprize TG, Hynynen K, Rutka JT. Enhanced delivery of gold nanoparticles with therapeutic potential into the brain using MRI-guided focused ultrasound. 2012; 8:1133–1142.
10. Liu H-L, Hua M-Y, Yang H-W, Huang C-Y, Chu P-C, Wu J-S, Tseng I-C, Wang J-J, Yen T-C, Chen P-Y, Wei K-C. Magnetic resonance monitoring of focused ultrasound/magnetic nanoparticle targeting delivery of therapeutic agents to the brain. Proc Natl Acad Sci U S A. 2010; 107:15205–10. [PubMed: 20696897]
11. Mulik RS, Bing C, Ladouceur-Wodzak M, Munaweera I, Chopra R, Corbin IR. Localized delivery of low-density lipoprotein docosahexaenoic acid nanoparticles to the rat brain using focused ultrasound. Biomaterials. 2016; 83:257–268. [PubMed: 26790145]
12. Baker SJ, Ellison DW, Gutmann DH. Pediatric gliomas as neurodevelopmental disorders. Glia. 2016; 64:879–895. [PubMed: 26638183]
13. Aryal M, Vykhodtseva N, Zhang YZ, Park J, McDannold N. Multiple treatments with liposomal doxorubicin and ultrasound-induced disruption of blood-tumor and blood-brain barriers improve outcomes in a rat glioma model. J Control Release. 2013; 169:103–111. [PubMed: 23603615]
14. Nance E, Timbie K, Miller GW, Song J, Louttit C, Klibanov AL, Shih T-Y, Swaminathan G, Tamargo RJ, Woodworth GF, Hanes J, Price RJ. Non-invasive delivery of stealth, brain-penetrating nanoparticles across the blood-brain barrier using MRI-guided focused ultrasound. J Control Release. 2014; 189:123–132. [PubMed: 24979210]
15. Diaz RJ, McVeigh PZ, O'Reilly MA, Burrell K, Bebenek M, Smith C, Etame AB, Zadeh G, Hynynen K, Wilson BC, Rutka JT. Focused ultrasound delivery of Raman nanoparticles across the blood-brain barrier: Potential for targeting experimental brain tumors. Nanomedicine Nanotechnology, Biol Med. 2014; 10:1075–1087.
16. Yang FY, Wang HE, Liu RS, Teng MC, Li JJ, Lu M, Wei MC, Wong TT. Pharmacokinetic Analysis of 111In-labeled liposomal doxorubicin in murine glioblastoma after blood-brain barrier disruption by focused ultrasound. PLoS One. 2012; 7:1–7.
17. Choi HS, Liu W, Misra P, Tanaka E, Zimmer JP, Itty Ipe B, Bawendi MG, Frangioni JV. Renal clearance of nanoparticles. Nat Biotechnol. 2007; 25:1165–1170. [PubMed: 17891134]
18. Chen T, Xu S, Zhao T, Zhu L, Wei D, Li Y, Zhang H, Zhao C. Gold nanocluster-conjugated amphiphilic block copolymer for tumor-targeted drug delivery. ACS Appl Mater Interfaces. 2012; 4:5766–5774. [PubMed: 23043448]

19. Longmire M, Choyke PL, Kobayashi H. Clearance properties of nano-sized particles and molecules as nanomedicine. Nanomedicine. 2008; 3:703–717. [PubMed: 18817471]
20. Zhang XD, Wu D, Shen X, Liu PX, Fan FY, Fan SJ. In vivo renal clearance, biodistribution, toxicity of gold nanoclusters. Biomaterials. 2012; 33:4628–4638. [PubMed: 22459191]
21. Zhao Y, Sultan D, Detering L, Luehmann H, Liu Y. Facile synthesis, pharmacokinetic and systemic clearance evaluation, and positron emission tomography cancer imaging of 64Cu–Au alloy nanoclusters. Nanoscale. 2014; 6:13501–13509. [PubMed: 25266128]
22. Zhao Y, Detering L, Sultan D, Cooper ML, You M, Cho S, Meier SL, Luehmann H, Sun G, Rettig M, Dehdashti F, Wooley KL, DiPersio JF, Liu Y. Gold nanoclusters doped with $^{64}$Cu for CXCR4 positron emission tomography imaging of breast cancer and metastasis. ACS Nano. 2016 acsnano. 6b01326.
23. Choi JJ, Pernot M, Small SA, Konofagou EE. Noninvasive, transcranial and localized opening of the blood-brain barrier using focused ultrasound in mice. Ultrasound Med Biol. 2007; 33:95–104. [PubMed: 17189051]
24. Chen H, Chen CC, Acosta C, Wu S-Y, Sun T, Konofagou EE. A new brain drug delivery strategy: focused ultrasound-enhanced intranasal drug delivery. PLoS One. 2014; 9:e108880. [PubMed: 25279463]
25. Hynynen K, McDannold N, Vykhodtseva N, Raymond S, Weissleder R, Jolesz Fa, Sheikov N. Focal disruption of the blood-brain barrier due to 260-kHz ultrasound bursts: a method for molecular imaging and targeted drug delivery. J Neurosurg. 2006; 105:445–54. [PubMed: 16961141]
26. Chen H, Konofagou EE. The size of blood-brain barrier opening induced by focused ultrasound is dictated by the acoustic pressure. J Cereb Blood Flow Metab. 2014; 34:1197–204. [PubMed: 24780905]
27. KBF, George, Paxinos. The mouse brain in stereotaxic coordinates. Gulf Professional Publishing; 2004.
28. Liu H-L, Fan C-H, Ting C-Y, Yeh C-K. Combining microbubbles and ultrasound for drug delivery to brain tumors: current progress and overview. Theranostics. 2014; 4:432–44. [PubMed: 24578726]
29. Chen H, Konofagou EE. The size of blood-brain barrier opening induced by focused ultrasound is dictated by the acoustic pressure. J Cereb Blood Flow Metab. 2014; 34:1197–204. [PubMed: 24780905]
30. Zhao Y, Sultan D, Detering L, Cho S, Sun G, Pierce R, Wooley KL, Liu Y. Copper-64-alloyed gold nanoparticles for cancer imaging: Improved radiolabel stability and diagnostic accuracy. Angew Chemie - Int Ed. 2014; 53:156–159.
31. Kovacs ZI, Kim S, Jikaria N, Qureshi F, Milo B, Lewis BK, Bresler M, Burks SR, Frank JA. Disrupting the blood–brain barrier by focused ultrasound induces sterile inflammation. Proc Natl Acad Sci. 2016 201614777.
32. Yang F-Y, Wang H-E, Lin G-L, Teng M-C, Lin H-H, Wong T-T, Liu R-S. Micro-SPECT/CT-based pharmacokinetic analysis of 99mTc-diethylenetriaminepentaacetic acid in rats with blood-brain barrier disruption induced by focused ultrasound. J Nucl Med. 2011; 52:478–484. [PubMed: 21321259]
33. Chung YH, Hsu PH, Huang CW, Hsieh WC, Huang FT, Chang WC, Chiu H, Hsu ST, Yen TC. Evaluation of prognostic integrin α2β1 PET tracer and concurrent targeting delivery using focused ultrasound for brain glioma detection. Mol Pharm. 2014; 11:3904–3914. [PubMed: 25153169]
34. Okada M, Kikuchi T, Okamura T, Ikoma Y, Tsuji AB, Wakizaka H, Kamakura T, Aoki I, Zhang M-R, Kato K. In-vivo imaging of blood-brain barrier permeability using positron emission tomography with 2-amino-[3-11C]isobutyric acid. Nucl Med Commun. 2015; 36:1239–48. [PubMed: 26397998]
35. Yang FY, Chang WY, Chen JC, Lee LC, Hung YS. Quantitative assessment of cerebral glucose metabolic rates after blood-brain barrier disruption induced by focused ultrasound using FDG-MicroPET. Neuroimage. 2014; 90:93–8. [PubMed: 24368263]

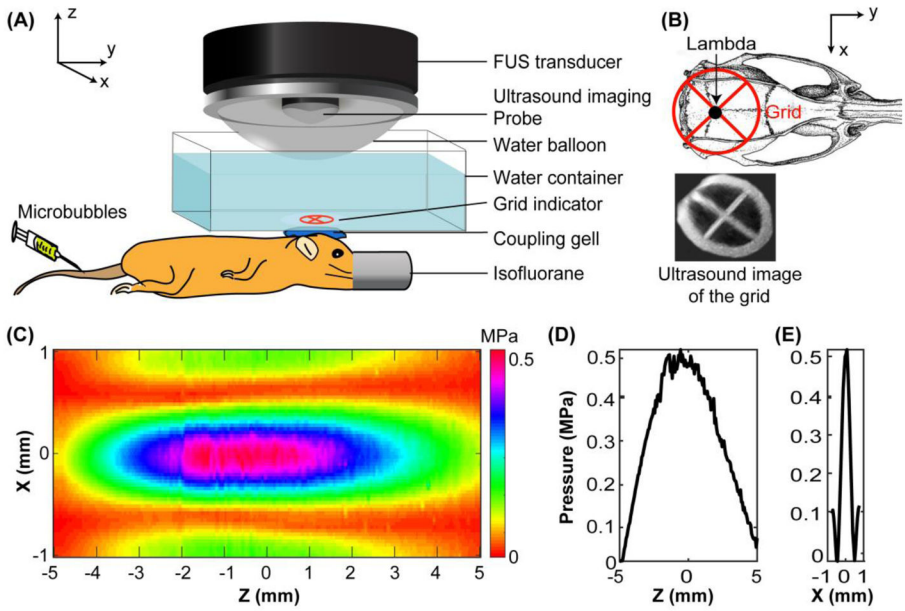


**Figure 1.**

(A) Illustration of the FUS treatment setup. (B) Illustration of FUS targeting of the pons with the assistance of a grid. The grid was placed on top of the mouse head with the center of the grid aligned visually with the lambda. B-mode images of the grid were obtained and reconstructed to 3D for the identification of the grid crossing point. The left pons was targeted based on its stereotactic location in reference to the lambda. (C) 2D pressure map of the FUS beam at the axial focal plane. (D) Axial and (E) lateral pressure profiles across the focus. The directions of the axes (X, Y, and Z) are added in (A) and (B) to help understand the positioning of C, D, and E with respect to the mouse.

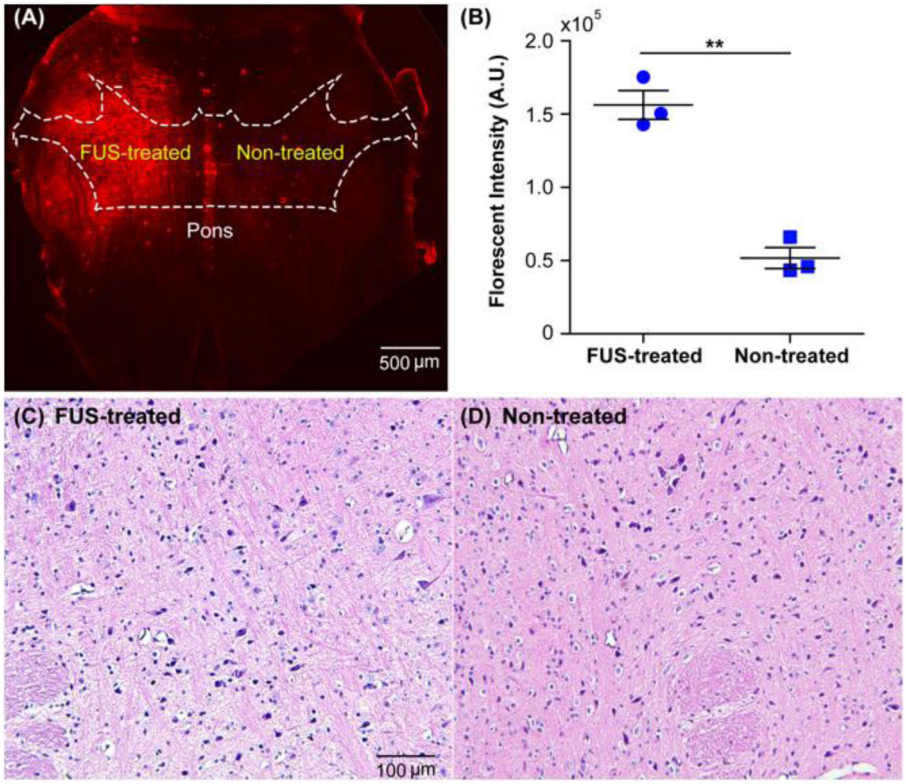


**Figure 2.**

FUS enhanced targeted delivery of the fluorescently-labeled dextran to the pons. (A) Representative fluorescence image of the pons in one horizontal section of an ex vivo mouse brain slice. The approximate location of the pons is illustrated by the white dash line in reference to the atlas of the mouse horizontal brain section [27]. The enhanced fluorescence signal observed on the FUS-treated left side of the pons compared with the non-treated right side of the pons confirmed the successful delivery of the dextran to the left pons. (B) Quantification of fluorescence intensities of the mouse brains in the whole group. Across the group, FUS significantly enhanced dextran delivery at the treated pons when compared with the non-treated control. (**: $P < 0.01$). Histological examinations of (C) the left treated pons and (D) the contralateral right non-treated pons by hematoxylin and eosin (H&E) staining.

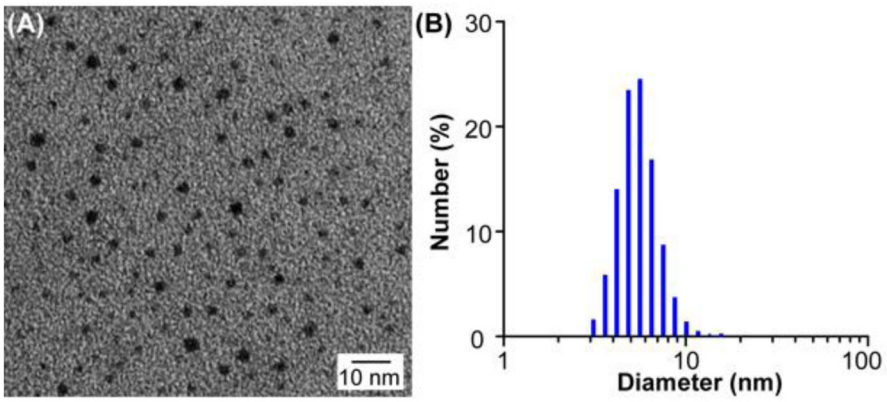


**Figure 3.**

Characterization of $^{64}$Cu-AuNCs. (A) Transmission electron microscopy image and (B) dynamic light scattering histogram of $^{64}$Cu-AuNCs show the prepared $^{64}$Cu-AuNCs had uniform size distribution.

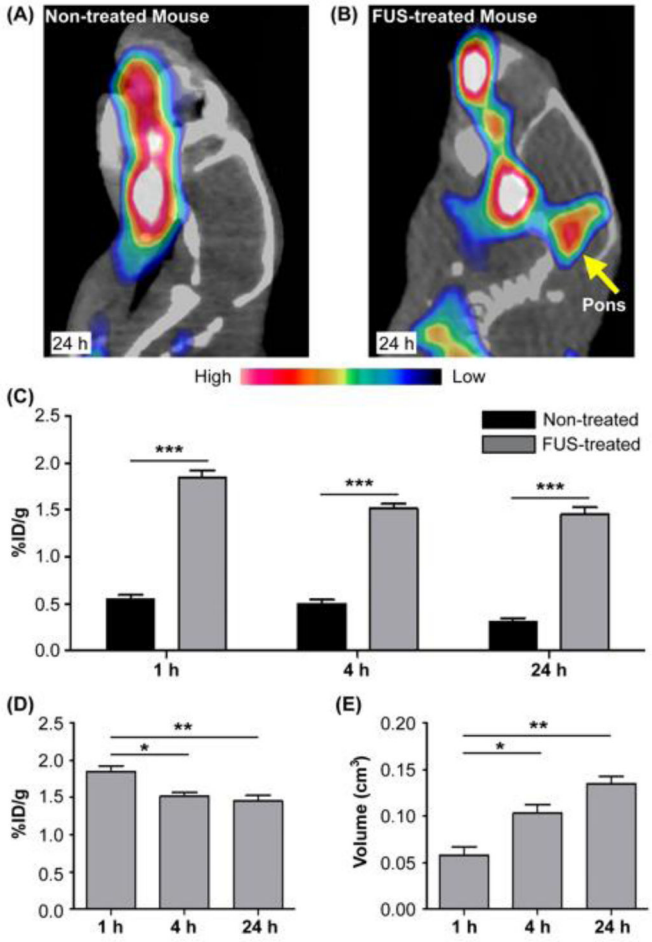


**Figure 4.**

Representative PET/CT images of non-treated (A) and FUS-treated (B) mouse brains at 24 h after intravenous injection of $^{64}$Cu-AuNCs. (C) Quantification of $^{64}$Cu-AuNCs brain uptakes in FUS-treated mice and non-treated mice at 1 h, 4 h, and 24 h post. FUS-treated mice had significantly higher brain uptake of the $^{64}$Cu-AuNCs at all three time points. Comparison of the $^{64}$Cu-AuNCs brain uptakes (D) and diffusion volume (E) at 1 h, 4 h, and 24 h post injection for the FUS-treated mice. The amount of radioactivity retained in the mouse brains decreased over time but the diffusion volume increased over time (*:$P < 0.05$, **: $P < 0.01$, ***: $P < 0.005$).

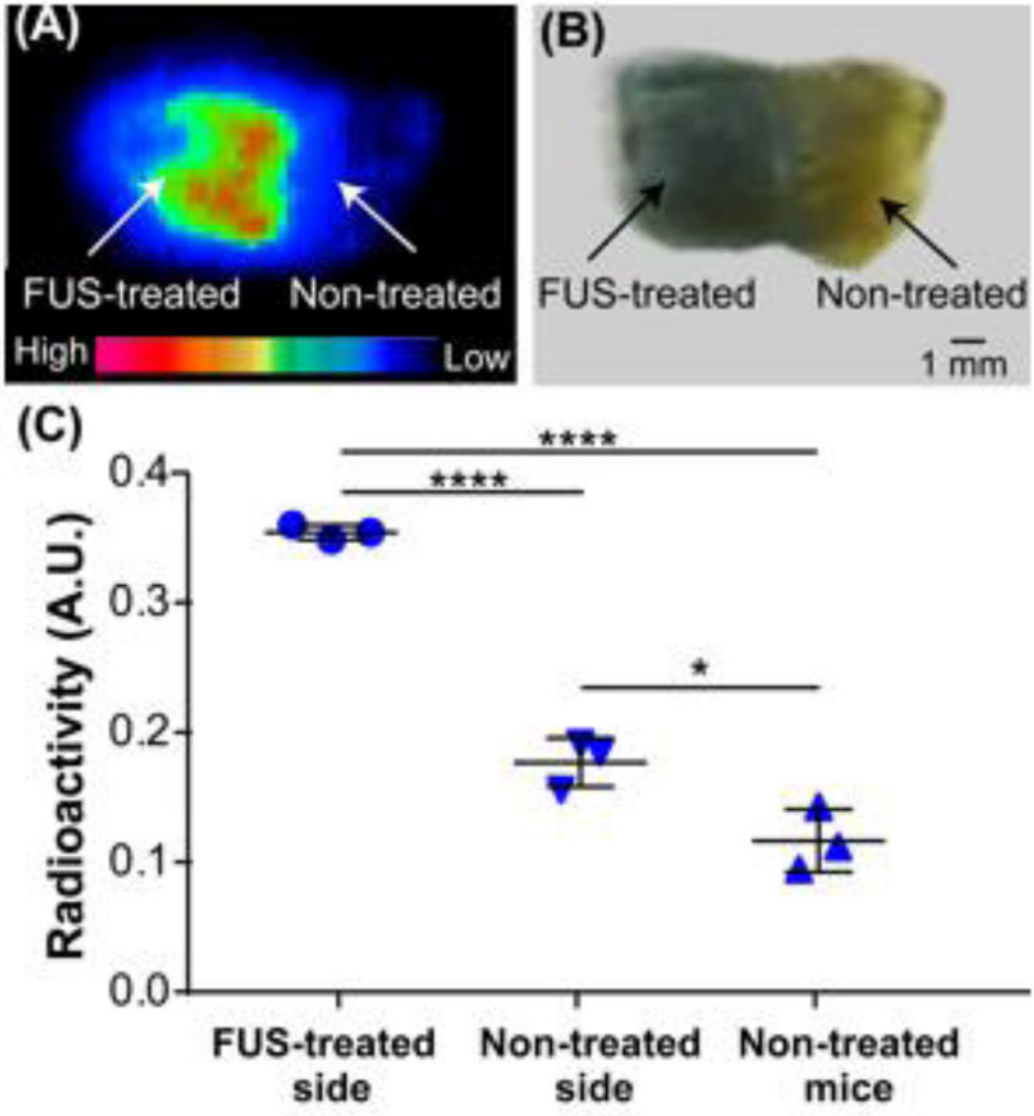


**Figure 5.**

(A) Representative autoradiograph of $^{64}$Cu-AuNCs in coronal brain slices at 24 h post-injection, indicating the localized delivery of $^{64}$Cu-AuNCs inside the FUS-treated left side of the mouse brain. (B) Photograph of the brain slice shown in (A). (C) Quantification of radioactivity uptake at the FUS-treated left side, the contralateral non-treated right side of the brain slices, and the brain slices prepared from non-treated mice. (*:$P < 0.05$, ****: $P < 0.0001$).

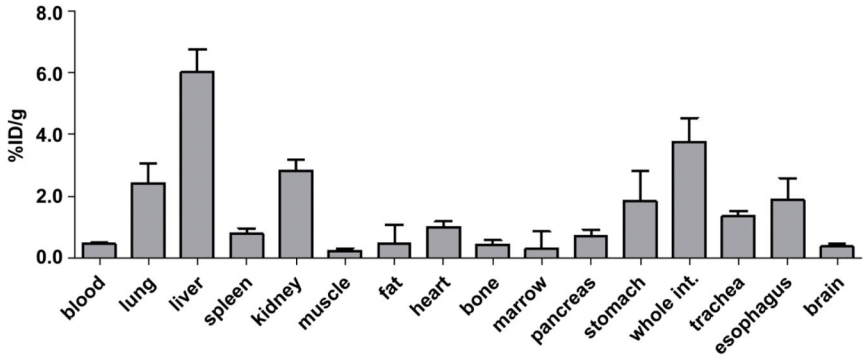


**Figure 6.**
Biodistribution of $^{64}$Cu-AuNCs measured at 24 h post-injection.

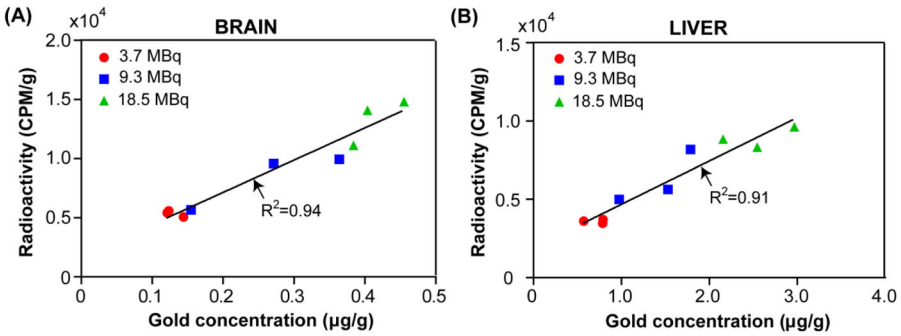


**Figure 7.**

Correlation between $^{64}$Cu radioactivity measured by gamma counting and Au concentration measured by ICP-MS of the same (A) brain and (B) liver samples with different $^{64}$Cu-AuNCs concentrations (3.7 MBq, 9.3 MBq, and 18.5 MBq, n=3/group).